Mapping Lipid Species Remodeling in High Fat Diet-Fed Mice: Unveiling Adipose Tissue Dysfunction with Raman Microspectroscopy

Elnaz Sheikh[1], Qianglin Liu[2], David Burk[3], Zehua Zhou[4], Xing Fu[2,*], William N Beavers[4,*], Manas Ranjan Gartia[1,*]

[1]Department of Mechanical and Industrial Engineering, Louisiana State University, Baton Rouge, LA 70803, USA.

[2]LSU AgCenter, School of Animal Sciences, Louisiana State University, Baton Rouge, LA 70803, USA.

[3]Pennington Biomedical Research Center, Baton Rouge, LA 70808, USA

[4] Department of Pathology, Microbiology, and Immunology, Vanderbilt University Medical Center, Nashville, Tennessee, United States of America.

Corresponding authors: xfu1@agcenter.lsu.edu (X.F.); wbeavers@lsu.edu (W. N. B); mgartia@lsu.edu (M.R.G.)

Abstract

Dysregulated lipid metabolism in obesity leads to adipose tissue expansion, a major contributor to metabolic dysfunction and chronic disease. Lipid metabolism and fatty acid changes play vital roles in the progression of obesity. In this work, Raman techniques coupled with histochemistry imaging methods were employed to characterize the effects of high-fat diet (HFD) feeding on various types of adipose tissue in mice. After six weeks of high-fat diet (HFD) feeding, our findings showed hypertrophy, elevated collagen levels, and increased macrophage presence in the adipose tissues of the HFD group compared to the low-fat diet (LFD) group. Statistical analysis of Raman spectra revealed significantly lower unsaturated lipid levels and higher saturated lipid levels in different fat pads (brown adipose tissue (BAT), subcutaneous white adipose tissue (SWAT), and visceral white adipose tissue (VWAT)) with HFD. Raman images of adipose tissues were analyzed using Empty modeling and DCLS methods to spatially profile unsaturated and saturated lipid species in the tissues. It revealed elevated levels of ω3, ω6,

cholesterol, and triacylglycerols in BAT adipose tissues of HFD compared to LFD tissues. These findings indicated that while cholesterol and triacylglycerol levels have risen in the SWAT and VWAT adipose tissues of the HFD group, the levels of ω3 and ω6 have decreased following the HFD. The study showed that as an effective and non-destructive method, Raman spectroscopy and microscopy provided invaluable information at the molecular level for investigating lipid species remodeling and spatial mapping of adipose tissues during HFD.
Key Words: Adipose tissues, High-fat diet, Lipid alterations, Raman spectroscopy

INTRODUCTION

Obesity occurs due to excessive energy intake and inadequate energy usage. Obesity is correlated with many diseases, such as insulin resistance, diabetes mellitus, cardiovascular disease, several forms of cancers, various musculoskeletal disorders, poor mental health, and a low-grade inflammatory state [1, 2]. Adipose tissues are the primary tissues affected by overweight and obesity [3, 4]. Moreover, adipose tissue dysfunctions can affect whole-body functions and induce obesity-associated diseases [5]. Hence, the metabolic homeostasis of the body significantly relies on the ability of adipose tissue remodeling as a reaction to extreme calorie intake.

Adipose tissues are generally divided into four types: white (WAT), brown (BAT), beige, and pink [5]. Each type of adipose tissue has its function. For instance, white adipocytes store excess energy in the form of triglycerides, while brown adipocytes dissipate energy from triglycerides through heat production [6]. White adipose tissue (WAT) has an endocrine function, releasing hormones like leptin, adiponectin, and proinflammatory cytokines. These levels rise in obesity and contribute to obesity-related metabolic diseases. In contrast, brown adipose tissue (BAT) and beige adipose tissue are specialized in burning energy. Their activity helps prevent obesity and metabolic disorders [3]. Adipose tissue consists of lipid-filled mature adipocytes and various stromal cells, including preadipocytes, fibroblasts, endothelial cells, and immune cells. Its primary function is lipid storage, crucial in maintaining energy homeostasis [7, 8]. The primary components of lipids are fatty acids (FAs); they are metabolized significantly by

adipose tissue, skeletal muscle, and the liver compared to other tissues. [9]. Among all fatty acids (FAs), ω-6 and ω-3 represent two distinct classes. Mammalian cells lack the ω-3 desaturase enzyme, making them incapable of converting ω-6 to ω-3 fatty acids. As a result, ω-6 and ω-3 fatty acids are not interchangeable (interconvertible), and they exhibit distinct metabolic and functional characteristics, often leading to significant opposing physiological effects. Thus, maintaining an appropriate balance of these fatty acids in the diet is critical due to their impact on health [10]. ω-6 and ω-3 fatty acids can be differentiated based on the first double bond location, counting from the methyl end of the fatty acid molecule. The ω-3 and ω-6 PUFA families are vital fatty acids in the health of humans, and they must be gained through dietary consumption. An example of ω-6 fatty acid includes Linoleic acid (LA) (18:2ω-6), while α-Linoleic Acid (α-LA) (18:3ω-3) is an example of ω-3 fatty acids [6]. Mammals lack Δ12- and Δ15-desaturases, making them incapable of synthesizing Linoleic acid and α-Linoleic acid. LA and α-LA can be metabolized to longer chains metabolites, more polyunsaturated fatty acids (PUFAs), through an identical pathway, additional elongation and desaturation processes [11]. α-LA is converted to eicosapentaenoic acid (EPA) (20:5n-3), docosapentaenoic acid (22: 5*n*-6), and then docosahexaenoic acid (DHA) (22:6n-3), while LA is transformed to arachidonic acid (20:4n-6) [11, 12]. Arachidonic acid (AA) acts as the building block for potent signaling molecules called eicosanoids, including prostaglandins (PG), thromboxanes, and leukotrienes. PG1, PG2, and PG3 are three various types of PG; each has its effects on the body. PG1 has an anti-inflammatory effect, facilitating the body's recovery after injury, while PG2 has an inflammatory effect, promoting inflammation, vasoconstriction, and blood clotting. PG3 plays a complex role in the body, but its most notable function is countering the inflammation triggered by PG2. This balancing act starts with dihomo-γ-linolenic acid (DGLA), an intermediate molecule in the omega-6 pathway. DGLA can be converted into either anti-inflammatory PG1 or arachidonic acid, the precursor for the proinflammatory PG2. This conversion depends on two enzymes: Δ5-desaturase and Δ6-desaturase. Interestingly, both enzymes are sensitive to factors like diet and inflammation itself, potentially influencing the production of these opposing prostaglandins. This interplay between enzymes, metabolites, and external factors highlights the potential role of diets in modulating inflammatory processes. Diets rich in omega-3 fats

steer dihomo-γ-linolenic acid (DGLA) down an anti-inflammatory pathway, using the Δ5-desaturase enzyme to create the helpful PG1. In contrast, diets heavy in omega-6 fats push DGLA towards a proinflammatory route, turning it into arachidonic acid (AA), which fuels the production of inflammatory PG2 [11, 13].

The Δ6-desaturase enzyme uses Linoleic, α-Linolenic, and Oleic acids as substrates. Consequently, the ω-6, ω-3, and ω-9 fatty acid families compete with each other for the pathway of desaturation-elongation. The ideal substrate for Δ6-desaturase is α-Linolenic acid, which is followed by Linoleic acid and Oleic acid. However, the ω-6 fatty acid metabolism is quantitatively more significant since the human diet is richer in linoleic acid than α-Linolenic acid [11].

In addition, Lipid droplets store energy as triacylglycerol, forming through the esterification of fatty acids and α-glycerophosphate. Triacylglycerols are components of other lipids, such as phospholipids [8]. The composition of FAs in cellular phospholipids and triacylglycerol (TAG) indicates their dietary intake [14]. Moreover, research indicates obesity leads to the dysfunction of adipocytes through the imbalance of cholesterol [15]. Comparatively, adipocytes from obese individuals hold more cholesterol than their lean counterparts. The amount of cholesterol rises with the size of adipocytes, implying that expanded adipocytes have excess cholesterol [15]. The amount of cholesterol and triacylglycerols in the lipid droplet varies proportionally to each other [16]. Thus, due to the significance of fatty acids, triacylglycerols, and cholesterol and their impact on adipose tissue functionality, adipose tissues have gained lots of attention, and there is a need for novel analytical methods to characterize and assess them.

Currently, various methods have been developed to detect lipids, including mass spectrometry (MS) [17, 18], and fluorescence assays [19, 20]. Nevertheless, many of these approaches are invasive, requiring rigorous sample preparation. Furthermore, this sample preparation process could destroy the three-dimensional structure of cells and tissues [21]. In this manner, non-destructive optical approaches have been used for studying cells and tissues.

Further, immunohistochemistry (IHC) is the widely semi-quantitative applied technique for biomarkers detection in clinical samples [22]. As a conventional method, this technique enables researchers to visually examine the morphology of tissue, cell types, and subcellular structures by staining with endogenous chemicals to form colored compounds. However, IHC is limited to probing only one or a few targets simultaneously in a sample [22, 23], and some chemicals cannot be applied in this method, restricting its application [22]. Confocal Raman spectroscopy and microscopy have emerged as powerful tools for studying molecular-level chemical composition changes within tissues, particularly in biological samples like the brain [24, 25], heart [26], and kidneys [27] to probe cells [28], proteins [29], and lipids [30]. Raman spectroscopy and microscopy are promising methods because they are non-destructive, label-free, relatively rapid, and require minimal sample preparation [3, 31]. Raman microscopy can also provide spatial mapping information of the cells and tissues [32], which cannot be achieved with other destructive methods like LC-MS [33]. The Raman spectra of tissues and cells comprise distinct bands associated with lipids owing to the significant Raman scattering cross-section of certain lipids, which is attributed to the long non-polar acyl chains in their structures. As a result, these lipid bands are commonly detected in Raman spectra and often serve as convenient markers for pathology [30]. While the Raman spectra of different lipids show some similarities, each lipid has some distinct characteristics, making its spectrum unique [34]. In lipid species, Raman bands are seen in both the fingerprint (400–1800 cm^{-1}) and higher wavenumber (2800–3800 cm^{-1}) region [30]. Commonly, lipids' characteristics arising from their hydrocarbon chains are detected in Raman signal ranges of 1200–1050 cm^{-1} representing the C–C stretching, the 1250–1300 cm^{-1} range corresponding to CH_3 scissoring and twisting, and the 1400–1500 cm^{-1} range associated with CH_2 scissoring and twisting. In the higher wavenumber of the spectrum, prominent Raman signals emerge within the range of 2800–3100 cm^{-1}, which is assigned to the stretching of C–H bonds in the lipids [24].

Using Raman spectroscopy and microscopy, other researchers have shown differences at the molecular level between HFD and LFD-fed mice. However, the application of Raman microscopy for profiling ω-3 and ω-6 species in the adipose tissues is scarcely reported [3, 35,

36]. This paper used Raman microspectroscopy to investigate the lipid metabolism and biochemical changes of the three adipose tissues (VWAT, SWAT, and BAT). We performed statistical analysis using Empty modeling and DCLS methods on the Raman images to obtain a detailed distribution of lipids in adipose tissue. In addition, Raman spectroscopy data were analyzed using unsupervised principal component analysis (PCA). The composition analysis of adipose tissues revealed that the lipid species from ω-3 and ω-6 groups were upregulated in adipose tissues of HFD mice.

EXPERIMENTAL METHODS

Materials

α-Linoleic acid (CAS # 822-18-4), Docosahexaenoic acid (CAS # 6217-54-5), Docosapentaenoic acid (CAS # 24880-45-3), Eicosapentaenoic acid (CAS # 10417-94-4), Stearidonic acid (CAS # 20290-75-9), Arachidonoic acid (CAS # 506-32-1), Linoleic Acid (CAS # 60-33-3), Oleic acid (CAS # 112-80-1), and Cholesterol (CAS # 57-88-5), Cholesteryl palmitate (CAS # 601-34-3), 1,2-Dipalmitoyl-sn-glycero-3-phosphate sodium salt (CAS # 169051-60-9), and Glyceryl tripalmitate (CAS # 555-44-2) were obtained from Cayman Chemical.

Preparation of brown and white adipose tissues (Animal Model)

C57BL/6 male mice (n=3) per group of high-fat diet and low-fat diet were used in this study, and animal experimentation was approved by the Louisiana State University's Institutional Animal Care and Use Committee (Protocol # 21-153). Starting at the age of 6 weeks, mice were fed with a regular diet containing 13.4% calories (LabDiet #5001) and a high-fat diet (HFD) containing 60.3% calories (Teklad #TD.06414) for another 6 weeks to generate the lean mice and obese mice respectively. The lean and obese mice were euthanized and the brown adipose tissue (BAT) from interscapular area, the subcutaneous white adipose tissue (SWAT) from inguinal area and visceral white adipose tissue (VWAT) from epididymal area were carefully collected with forceps and surgical scissors freshly or snap frozen with liquid nitrogen then stored at -80 ℃ for further analysis. For each group of high-fat diet and low-fat diet mice, (n=3) tissues for BAT, (n=3) tissues for SWAT, and (n=3) tissues for VWAT were used for evaluation using each method.

Tissue Preparation for Raman imaging

For preparation of Formalin-Fixed Paraffin-Embedded (FFPE) samples, first tissues were harvested and stored at -80˚ C. Next, frozen tissues were fixed in 4% PFA immediately after removal from the -80˚ C freezer for 24 hours. After formalin fixation, adipose tissues were placed in cassettes and processed with a Sakura VIP-6 Tissue Tek (Sakura Finetek, USA). Embedded tissues were sectioned at 5 µm, mounted on metal slide, and dried overnight at room temperature. For the imaging of fresh samples, whole mount tissues were harvested and stored at -80˚ C and prior to application, frozen tissues were thawed.

Histology

For histological assessment, we stained thin tissue slices with hematoxylin and eosin (H&E) dye using an automated system (Leica ST5020/CV5030). This process employed specific solutions for both dyes (Eosin Phloxine 515 and SelecTech Hematoxylin 560) and included a bluing step. The stained slides were then viewed with specialized software (NDP.view2) and analyzed using ImageJ software for further insights.

Picrosirius red staining

Prior to paraffin processing, frozen tissues were thawed in 4% PFA at room temperature for 24 hours and embedded in paraffin. After removing the wax (dewaxing) and rehydrating the tissue slices, we stained them using a special kit (picrosirius red, Polysciences, Inc., #24901) designed for both fixed and frozen samples. We then used a microscope equipped with polarized light (Leica DM6B, 10x/0.3 NA objective) to see how the collagen fibers were arranged (birefringence) and captured images with a digital camera (Leica DFC450).

Immunohistochemistry imaging

To identify macrophages in tissue samples, we used an automated immunohistochemistry (IHC) system (Leica BOND-MAX) with a custom protocol (Protocol F). This protocol involved incubating the tissue with a special antibody against macrophages (anti-Iba1, 1:1500 dilution, Fujifilm Wako Chemicals, 019-19741) for 60 minutes, followed by a 20-minute heat treatment step (ER1 HIER) and a detection step using a kit (Polymer Refine Detection kit). After staining, the slides were dehydrated, covered, and scanned using a high-resolution microscope

(Hamamatsu Nanozoomer) with a 20x objective (0.8 NA). Images were captured using specialized software (NDP.view2).

Raman Spectroscopy and microscopy experiments

To acquire Raman spectra, BAT, SWAT, and VWAT tissues mounted on metal slides were analyzed using a Renishaw inVia Reflex spectrometer (785 nm laser, 50XL air objective, 1200 grating). In each group of collected tissues (n=3), for both high-fat diet and low-fat diet tissues, a total of 30 spectra were collected. Spectra were recorded at 100% power (180mW), 10 s exposure, and 100-3200 cm^{-1} range. Liquid/powder lipid standards were analyzed similarly with 10% power (18mW). Raman images of FFPE tissues were acquired using StreamHR mode (same laser/objective) at 50% power (90mW), 0.2s exposure, 1200 cm^{-1} center. Each image of FFPE sample yielded 4675 spectra with the step size of 6 µm by 6 µm along x and y axes. Raman images of fresh sample from whole mount tissues were acquired using StreamHR mode (same laser/objective) at 100% power (180mW), 0.4s exposure, 1200 cm^{-1} center. Each image of FFPE sample yielded 874 spectra. Each image of FFPE sample yielded 874 spectra with the step size of 4 µm by 4 µm along x and y axes. The total area of 152 µm × 92 µm was imaged in each fresh sample.

Raman analysis – Empty Modeling and Direct Classical Least Square.

Both Empty modeling and Direct Classical Least Square (DCLS) were performed using Renishaw's WiRE 4.4 software. *Empty modeling:* This unsupervised method employs multivariate curve resolution alternating least squares (MCR-ALS) to iteratively decompose Raman spectra into pure components (**C**) for each pixel in the map, optimizing the fit ($\mathbf{X} = \mathbf{C}*\mathbf{S}^T + \mathbf{E}$) until desired variance is achieved. *DCLS:* This supervised method requires known component spectra (**S**) and utilizes Beer's Law ($\mathbf{D} = \mathbf{C}*\mathbf{S}^T + \mathbf{E}$) to generate quantitative maps of their distribution and concentration (**C**) within the sample. Here, **E** represents the error, T is the transpose of the matrix. Associated images show component distribution from low to high concentration. If the Raman image has $M \times N$ pixels, and each spectra has P number of unique components (example of 4 components will be, protein, DNA, lipids, and collagen), then $\mathbf{D} = M \times N$, $\mathbf{C} = M \times P$, and $\mathbf{S} = N \times P$.

Statistical analysis and data processing:

For statistical analysis, ten Raman spectra were acquired per group in extended mode using Renishaw's WiRE 4.4 software. The software's "Intelligent fitting" was also used to subtract baselines from all spectra. OriginLab software (OriginLab, Northampton, MA) facilitated plotting the spectra, data processing, and principal component analysis. DCLS and Empty modeling methods were employed to generate mapping data. ImageJ 1.8 software assisted with the quantitative analysis of H&E, PSR, and IHC images. Specifically, the Adiposoft plugin within ImageJ measured cell number, area, and diameter in H&E images, averaging results across three replicates per group. For PSR and IHC images, the threshold method calculated the percentage area of collagen and crown-like structures. Finally, a two-tailed Student's t-test determined statistically significant differences (p-value).

Fatty acid extraction. Adipose tissue samples were suspended in 200 mL of 0.1 N HCl, 200 mL of methanol, and 600 mL of methyl tertbutyl ether (MTBE) to extract the fatty acids. The samples were subjected to multiple freeze/thaw cycles at -80 °C to lyse the cells and expose the cellular contents to the organic solvent. The organic and aqueous fractions were separated by centrifugation at maximum speed and 4 °C for 10 min. The MTBE layer (upper) was transferred to a clean glass tube for concentration. The aqueous fraction was extracted twice more with 600 mL of MTBE each time. All fractions were combined and dried under a stream of nitrogen gas at room temperature. Each sample was dissolved in 1.5 mL of 2:1 isopropanol:ethanol for LC-MS/MS analysis.

AMP+ derivatization. 10 mL of each sample was transferred to an LC-MS/MS vial insert and dried under a stream of nitrogen at room temperature. Each sample was derivatized with AMP+ as described in the kit instructions (AMP+ MaxSpec Kit, Cayman Chemical, Ann Arbor, MI) (reference Bollinger et al.). A calibration mixture of fatty acids was also derivatized for quantification and to confirm the appropriate retention times of each derivatized fatty acid. Briefly, all derivatization reagents were added to each sample and the samples were incubated for 30 min at 60 °C. After equilibrating to room temperature, the samples were analyzed by LC-MS/MS.

Protein isolation. Following extraction, proteins in the aqueous fraction were precipitated with 1 mL of ice cold acetone. The proteins were pelleted by centrifugation at maximum speed and 4

°C for 10 min. The proteins were suspended in 400 mL of 1 % SDS in PBS, sonicated twice with a probe sonicator, and incubated for 1 h at 70 °C. Proteins were quantified by BCA exactly as described in the kit instructions.

LC-MS/MS analysis. The samples were analyzed at the LSU School of Veterinary Medicine Mass Spectrometry Resource Center on a Shimadzu 8060NX triple quadrupole mass spectrometer interfaced with a Shimadzu Nexera XS 40 series UHPLC and Shimadzu CTO-40S column oven. 1 mL of each sample, blank, or standard mixture was analyzed in positive ionization mode. Chromatographic separation was achieved using a Phenomenex Kinetex C_8 (150 mm length, 2.1 mm internal diameter, 2.6 mm particle size, 100 Å pore size) column with a Phenomenex Security Guard C_8 (2.1 mm internal diameter) guard column. Mobile phase A was 0.1 % formic acid in water and mobile phase B was 0.1 % formic acid in acetonitrile. The column oven was set to 40 °C and the flow rate was set to 0.4 mL/min for the entire analysis. The starting condition was 45 % B, which was held for 1 min. The B mobile phase was then ramped to 50 % over the next 9 min. The column was washed at 99 % B for 5 min, then equilibrated to 45 % B for 5 min. All instrument voltages were determined and optimized empirically prior to the analysis. The AMP+ derivatized fatty acid *m/z* transitions were 471.3 to 183.1 for arachidonic acid, 447.3 to 183.1 for linoleic acid, 473.3 to 183.1 for dihomo-γ-linolenic acid, 449.3 to 183.1 for oleic acid, 469.3 to 183.1 for eicosapentaenoic acid, 495.3 to 183.1 for docosahexaenoic acid, 445.3 to 183.1 for γ-linolenic acid, and 445.3 to 183.1 for α-linolenic acid. Despite having the same *m/z* transition, we were able to baseline resolve γ-linolenic acid and α-linolenic acid chromatographically. A calibration line of each AMP+ derivatized fatty acid was used to quantify each sample. Each sample was normalized to total protein for differences in starting material.

RESULTS

Figure 1 depicts the schematic of the animal model employed for investigating the high-fat diet effect in different adipose tissues using Raman spectroscopy and microscopy. We further applied the immunohistochemistry method to evaluate the macrophage level of the tissues. Additionally, hematoxylin-eosin (H&E)-stained tissues and picrosirius red (PSR)-stained adipose tissues were used to assess morphology and collagen changes. This multimodal imaging enabled us to investigate structural and chemical modifications in the fatty tissues.

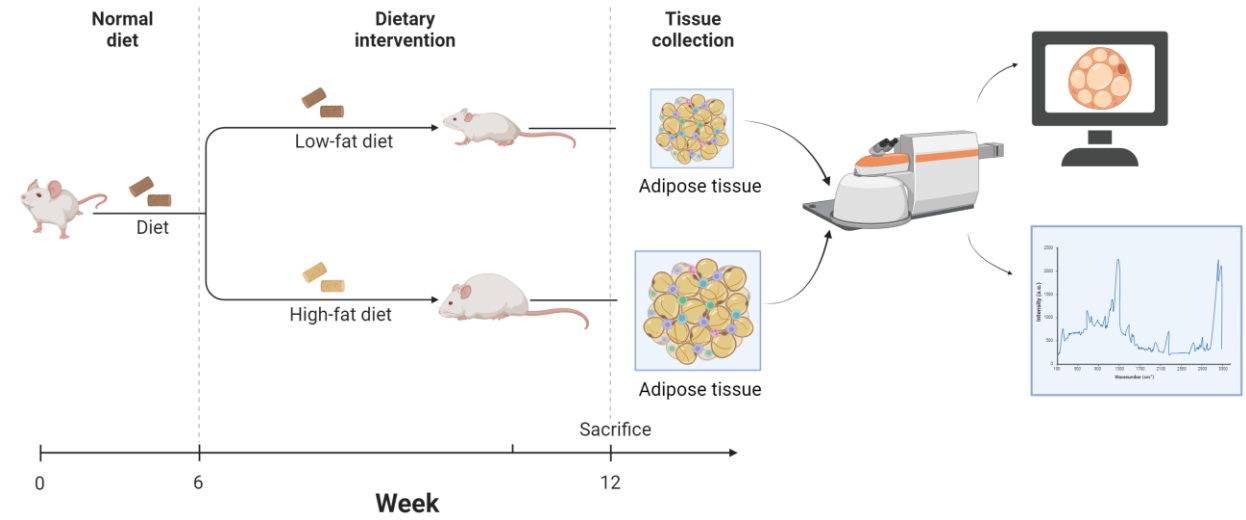

Figure 1. *Schematic showing the animal model applied to investigate a high-fat diet's effect in different adipose tissue types using Raman microspectroscopy.*

Figures 2A, 2D and 2G show H&E images and compare structural differences between LFD and HFD groups in the BAT, SWAT, and VWAT tissues. Obesity involves a significant expansion of adipose tissue, necessitating the remodeling and reorganization of the extracellular matrix (ECM). This process creates space for the enlargement of existing adipocytes (hypertrophy) and the generation of new ones through adipogenesis from precursor cells (hyperplasia) [37]. As can be seen, all types of adipose tissues in the HFD group underwent hypertrophy, as the area and diameter of adipocytes revealed an increase in the HFD groups compared to the LFD groups. **Figures 2B, 2C, 2E, 2F, 2H, and 2I** depict the mean area and diameter of the adipocytes calculated from the corresponding images. The BAT, SWAT, and VWAT tissues from HFD groups had significantly larger adipocyte area and diameter than those from LFD groups ($P < 0.001$). Additionally, both H&E images and the analysis of the images indicate that VWAT tissues are more affected by the HFD, showing a larger area and diameter compared to SWAT and BAT tissues in both HFD and LFD groups. Literature shows that both human and animal subcutaneous (SWAT) and visceral adipose tissues (VWAT) enlarge during obesity. However, the visceral adipose tissue primarily drives the metabolic effects linked to obesity, consistent with our findings [38].

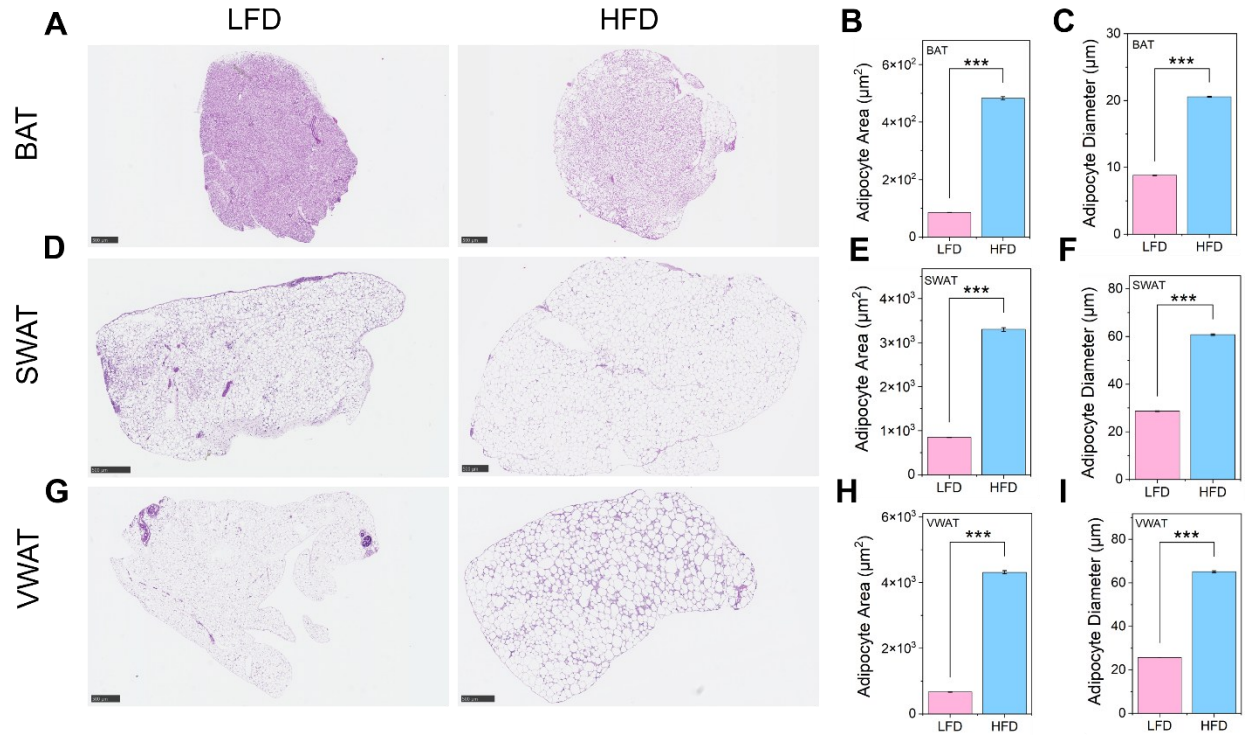

Figure 2. *Representative images of hematoxylin and eosin (H&E) stained tissues of LFD and HFD groups showing the structural differences of various lipid pads for (A) BAT, (D) SWAT, (G) VWAT. Comparison of adipocyte area and diameter between LFD and HFD groups calculated form their corresponding images for n=3 replicates. (B) and (c) BAT, (E) and (F) SWAT, (H) and (I) VWAT. The scalebar = 500 μm.*

The extracellular matrix (ECM) is vital for adipose tissue, providing structural support, protecting adipocytes from mechanical stress, and serving as a reservoir of growth factors and cytokines [39]. ECM remodeling is crucial for adapting to obesity-induced cellular changes, as adipocytes dynamically adjust their size. Excessive ECM deposition, or fibrosis, is a characteristic of obese adipose tissue resulting from chronic inflammation [39, 40]. Adipose tissue ECM mainly comprises collagens (I, II, III, and IV), fibronectin, and a small amount of laminin, playing a pivotal role in adipogenesis and tissue architecture [37, 41]. To evaluate the collagen level in LFD and HFD, we stained the adipose tissue with picrosirius red (PSR) [42]. **Figures 3A, 3D, and 3F** illustrate the PSR images of adipose tissue, indicating the higher collagen

level (red color) in HFD tissues compared to LFD tissues. **Figures 3B, 3E, and 3G** quantify the collagen level calculated from the corresponding PSR images. The results showed that the collagen level increased in the HFD group compared to the LFD group for all the fat pads: BAT (not significant), SWAT ($P < 0.05$), and VWAT ($P < 0.05$). **Figure 3C** compares the collagen levels of different fat pads in the LFD group. The collagen levels in VWAT and SWAT tissues were significantly higher compared to the BAT tissues ($P < 0.01$ for VWAT and $P < 0.001$ for SWAT). **Figure 3H** compares the collagen level of different fat pads in the HFD group. The collagen level in VWAT was the highest in the HFD group.

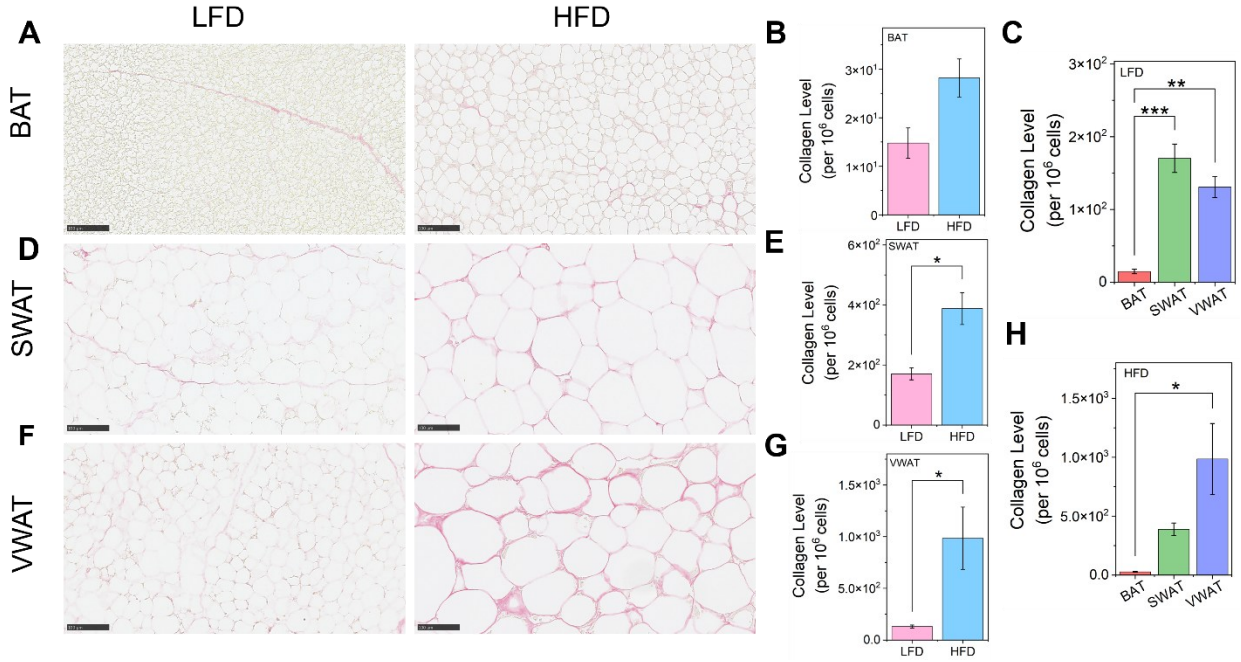

Figure 3. *Comparisons of picrosirius red (PSR) stained tissues showing the collagen level of different lipid pads between LFD and HFD groups. Bright-field images represent collagen levels in (A) BAT, (D) SWAT and (F) VWAT groups. Quantitative comparison of collagen level between LFD and HFD groups for (B) Bat, (C) LFD, (E) SWAT, (G) VWAT, and (H) HFD groups calculated from their corresponding images for n=3 replicates. The scalebar = 100 µm.*

Adipose tissue, primarily composed of adipocytes, is influenced by various cell types, including preadipocytes, lymphocytes, macrophages, fibroblasts, and vascular cells. Obesity increases macrophage infiltration in adipose tissue, contributing to inflammation [1]. To study

the cellular composition of adipose tissue before and after HFD, we evaluated both groups' macrophage levels. We used ionized calcium-binding adaptor molecule 1 (Iba1), a polypeptide selectively expressed in monocytic origin cells, for immunohistochemistry to assess macrophage levels in both LFD and HFD-fed adipose tissues [43]. **Figures 4A, 4D, and 4F** depict immunohistochemistry (IHC) images, in which Iba1 level and macrophages can be seen in brown color. As seen in the HFD group, VWAT tissues showed a greater number of macrophages aggregating in a crown-like structure. **Figures 4B, 4E, and 4G** show the macrophage level calculated from the corresponding images. The HFD group showed a significantly higher level of macrophages compared to the LFD groups for fat pads (BAT with $P < 0.01$, SWAT with $P < 0.05$, and VWAT with $P < 0.001$). In both LFD and HFD groups, BAT had the lowest Iba1 level. In the LFD group, SWAT had the highest Iba1 level (**Figure 4C**), whereas in the HFD group, VWAT had the highest Iba1 level (**Figure 4H**). Bruun et al. also reported a higher level of macrophages in VWAT tissues compared to the SWAT tissues [44].

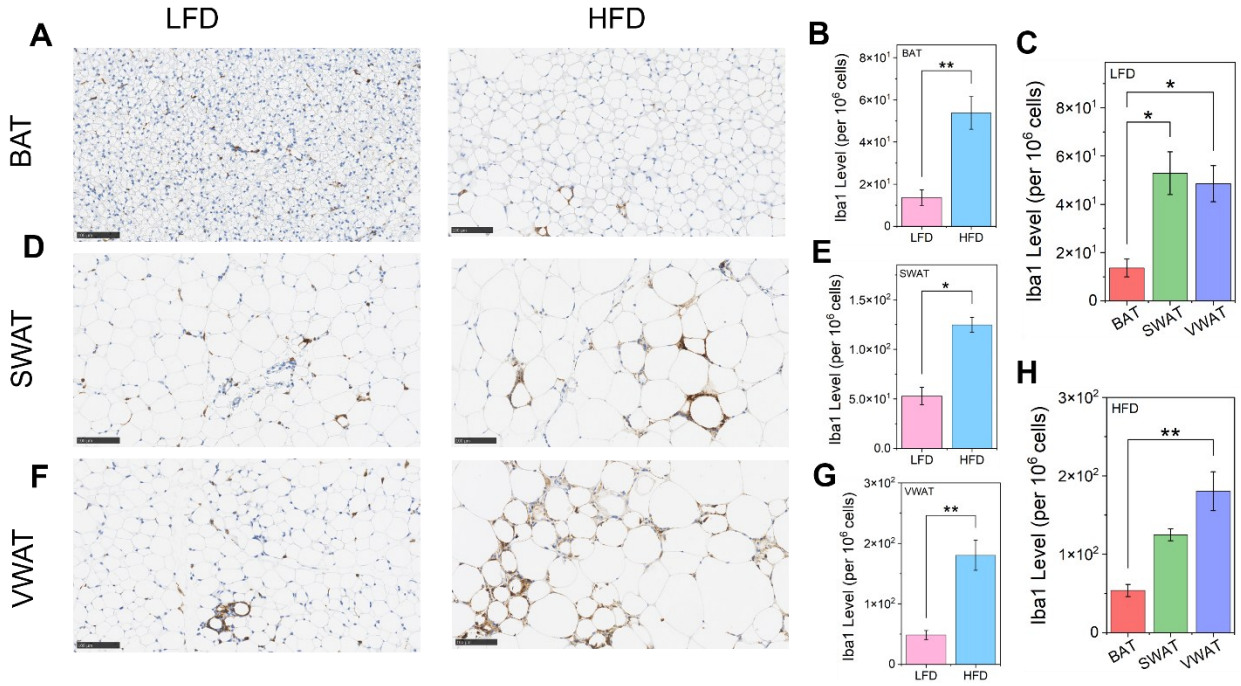

Figure 4. *Comparisons of immunohistochemical (IHC) stained tissues showing the Iba1 level of different lipid pads between LFD and HFD groups. Bright-field images represent the Iba1 level in (A) BAT, (D) SWAT and (F) VWAT groups. Quantitative comparison of Iba level between LFD and*

HFD groups for (B) Bat, (C) LFD, (E) SWAT, (G) VWAT, and (H) HFD groups calculated from their corresponding images for n=3 replicates. The scalebar = 100 µm.

The Raman spectra of adipose tissues from both LFD and HFD groups were acquired to demonstrate the biochemical variations in BAT, SWAT, and VWAT tissue. **Figures 5A-5C** compare both groups' mean Raman spectra for BAT, SWAT, and VWAT tissues. The Raman spectra of LFD and HFD tissues showed similar Raman peaks but different peak intensities. Raman bands around 871 cm^{-1} (glycerol), 1082 cm^{-1} (C-C stretching), 1121 cm^{-1} (C-N stretching mode), 1267 cm^{-1} (=C-H deformation mode), 1303 cm^{-1} (CH_2-CH_3 bending modes of lipids), 1440 cm^{-1} (CH_2-CH_3 scissoring mode), 1657 cm^{-1} (C=C stretching mode), 1748 cm^{-1} (C=O stretching vibrations), 2725 cm^{-1} (scissor bending modes of the CH_2), 2853 cm^{-1} (CH_2 symmetric stretching vibration), 2895 cm^{-1} (CH_2 asymmetric stretching vibration), 2928 cm^{-1} (CH_3 symmetric stretching vibration), 3010 cm^{-1} (CH_3 asymmetric stretching vibration) were identified [3, 30, 35, 36]. The exact peak positions of Raman spectra for each type of tissue in BAT, SWAT, and VWAT samples can be found in Table S1 (see *Supporting Information*).

Furthermore, we conducted principal component analysis (PCA) from the first two principal components on Raman spectra collected from each tissue in order to determine the significant variances existing in the obtained Raman data as a result of obesity. The Raman spectra in the low to high wavenumber range were acquired for each tissue type and then classified using PCA to generate the relevant principal component (PC) scores. As represented in the PCA plots, **Figures 5D-5F**, there are clear clusters between the HFD and LFD groups. In all groups, the first PC (BAT with PC1 94.6%, SWAT with PC1 97.6%, and VWAT with PC1 98.0%), revealed the majority of variance within the dataset, and the second PC (BAT with PC2 3.1%, SWAT with PC2 1.3%, and VWAT with PC2 0.9%), discriminates HFD groups from LFD groups. The first two PCs represent total variances of 97.7%, 98.9%, and 98.9% for BAT, SWAT, and VWAT tissues, respectively. Another distinction observed between the LFD and HFD groups relates to the peak intensity in the Raman spectra, indicating variations in molecular composition. Loading plots can be found in supporting information, Figure S1 to Figure S3.

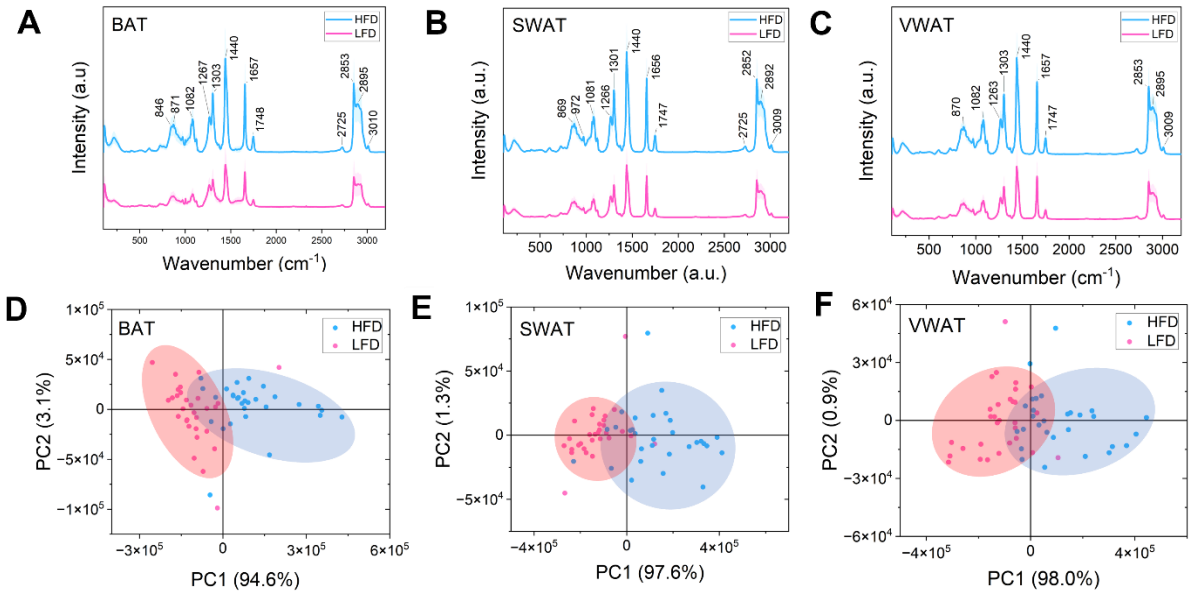

Figure 5. *Comparison of Raman spectra between LFD and HFD groups for (A) BAT, (B) SWAT, and (C) VWAT. The shaded areas surrounding the average spectra represent the standard deviation. Additionally, principal component analysis (PCA) score plots are presented for the first and second principal components, allowing differentiation between the LFD and HFD groups within individual adipose tissue types as shown in panels (D)* BAT*, (E)* SWAT*, and (F)* VWAT *respectively.*

All groups of tissues, BAT, SWAT, and VWAT, revealed distinct peaks at 1267 cm^{-1}, 1303 cm^{-1}, 1440 cm^{-1}, 1657 cm^{-1}, 2853 cm^{-1}, 2898 cm^{-1}, 3010 cm^{-1}, which are assigned to lipids. The intensity of these bands was used to calculate the level of lipid unsaturation by taking the ratio of unsaturated lipids (C=C) to saturated lipids (CH_2) bands. As the potential biomarker of lipid unsaturations, the selected ratio of Raman bands at 1267/1303 cm^{-1} (ratio of =CH in-plane deformation of lipids to CH_2 deformation of lipids), 1267/1440 cm^{-1} (ratio of =CH in-plane deformation of lipids to CH_3 deformation of lipids), 1657/1440 cm^{-1} (ratio of C=C stretch of lipids to CH_3 deformation of lipids), and 3010/1440 cm^{-1} (ratio of =C-H stretch of lipids to CH_3 deformation of lipids) were plotted in **Figures 6A**, **6B**, **6C**, **6E**, respectively. The results of the analysis, based on the 1267/1303 cm^{-1} and 1657/1440 cm^{-1} ratios, showed a significant decrease in the lipid unsaturation after HFD within BAT, SWAT, and VWAT tissues, **Figures 6A**

and 6C. Based on 1267/1440 cm^{-1} and 3010/1440 cm^{-1} ratio analysis, although the level of lipid unsaturation decreased in all tissue types after HFD, the difference calculated by the ratio of 1267/1440 cm^{-1} was significant for BAT after HFD, and the difference calculated by the ratio of 3010/1440 cm^{-1} was significant for BAT and VWAT tissues after HFD, **Figures 6B and 6E**. In addition, the peak at 2928 cm^{-1} is primarily associated with the CH3 stretching vibration of proteins. The intensity of the bands at 2853 cm^{-1} (CH_2 symmetric stretch of lipids), 2895 cm^{-1} (CH_2 asymmetric stretch of lipids), and 2928 cm^{-1} were used to assess the ratio of lipids over proteins. **Figure 6D** shows the ratio of 2853/2928 cm^{-1} Raman peaks with a significant increase in lipid-to-protein content in the BAT and a slight increase in the lipid-to-protein content of SWAT and VWAT tissues after HFD. Majka et al. also observed a decrease in the level of lipid unsaturation for TA PVAT, AA PVAT, and eWAT spectra of 18-week-old mice and an increase in lipid unsaturation for iBAT of 18-week-old mice from HFD compared to control after short-term HFD feeding. They also observed a decreasing trend for lipid unsaturation of HFD compared to the control group of 12-week-old mice for all these tissue types after long-term HFD feeding [35].

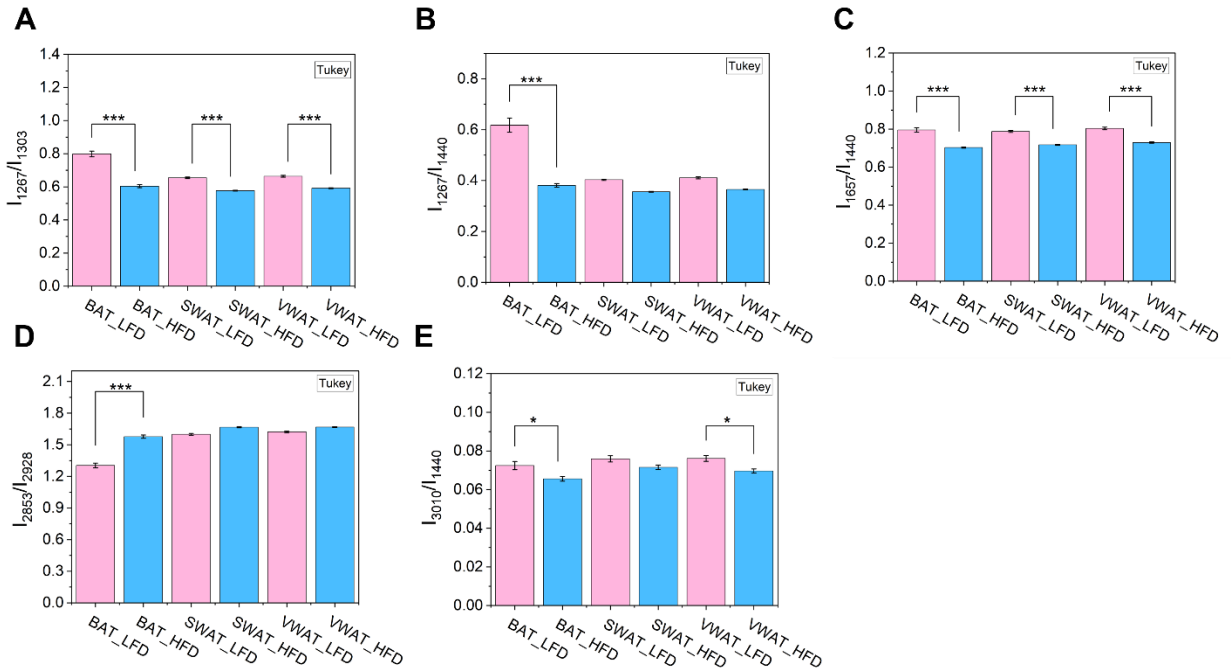

Figure 6. *Intensity ratios of specific Raman bands: (A)* 1267/1303 cm^{-1} (ratio of =CH in-plane deformation of lipids to CH_2 deformation of lipids) *(B)* 1267/1440 cm^{-1} (ratio of =CH in-plane deformation of lipids to CH_3 deformation of lipids) *(C)* 1657/1440 cm^{-1} (ratio of C=C stretch of lipids to CH_3 deformation of lipids) *(D)* 2852/2928 cm^{-1} (ratio of -CH_2 symmetric stretch of lipids to CH_3 stretch of proteins) *(E)* and 3010/1440 cm^{-1} (ratio of =C-H stretch of lipids to CH_3 deformation of lipids).

Raman images of the adipose tissues were collected for further spatial mapping and comparison of lipid profiles. Each Raman image was captured with a Raman center wavenumber of 1200 cm^{-1} and in the wavenumber range of 700-1400 cm^{-1}. First, we applied the Empty modeling method to compare the lipid profile in the adipose tissue. This method is beneficial when we do not know the chemical components inside the sample. The empty modeling method generates a few meaningful spectrums by the deconvolution of the Raman mapping image, showing the distribution of that significant spectrum. **Figure 7** illustrates the result of Raman mapping images analyzed using Empty modeling. **Figure 7A** shows the bright-field images of BAT, SWAT, and VWAT. Empty modeling identified two major components: component 1 (Figure 7D) and component 2 (**Figure 7E**). The corresponding Raman mapping

images for component 1 and component 2 for all fat pads are shown in **Figures 7B and 7C,** respectively. According to the Raman images, component 1 corresponds to the chemical species within the cytoplasm of the adipose tissues. In contrast, component 2 corresponds to the chemical species at the extracellular matrix of adipocytes in the adipose tissues. In the BAT-LFD tissue, component 1 comprises Raman bands at 844 cm^{-1}, 873 cm^{-1}, 892 cm^{-1}, 1002 cm^{-1}, 1032 cm^{-1}, 1064 cm^{-1}, 1082 cm^{-1}, 1130 cm^{-1}, 1301 cm^{-1}, 1368 cm^{-1}, 1439 cm^{-1}; component 2 comprises of Raman band at 1002 cm^{-1}, and 1033 cm^{-1}, 1302 cm^{-1}, 1446 cm^{-1}, 1601 cm^{-1}, 1658 cm^{-1}. In component 1, prominent peaks at 1301 cm-1 and 1440 cm-1 indicate the existence of lipids within the cytoplasm. The prominent peak at 1002 cm^{-1} in component 2 of all tissues signifies the presence of proteins in the membrane of adipose tissue [45]. Table S2 and Table S3 display all Raman bands corresponding to components 1 and 2 in BAT, SWAT, and VWAT tissues from LFD and HFD samples.

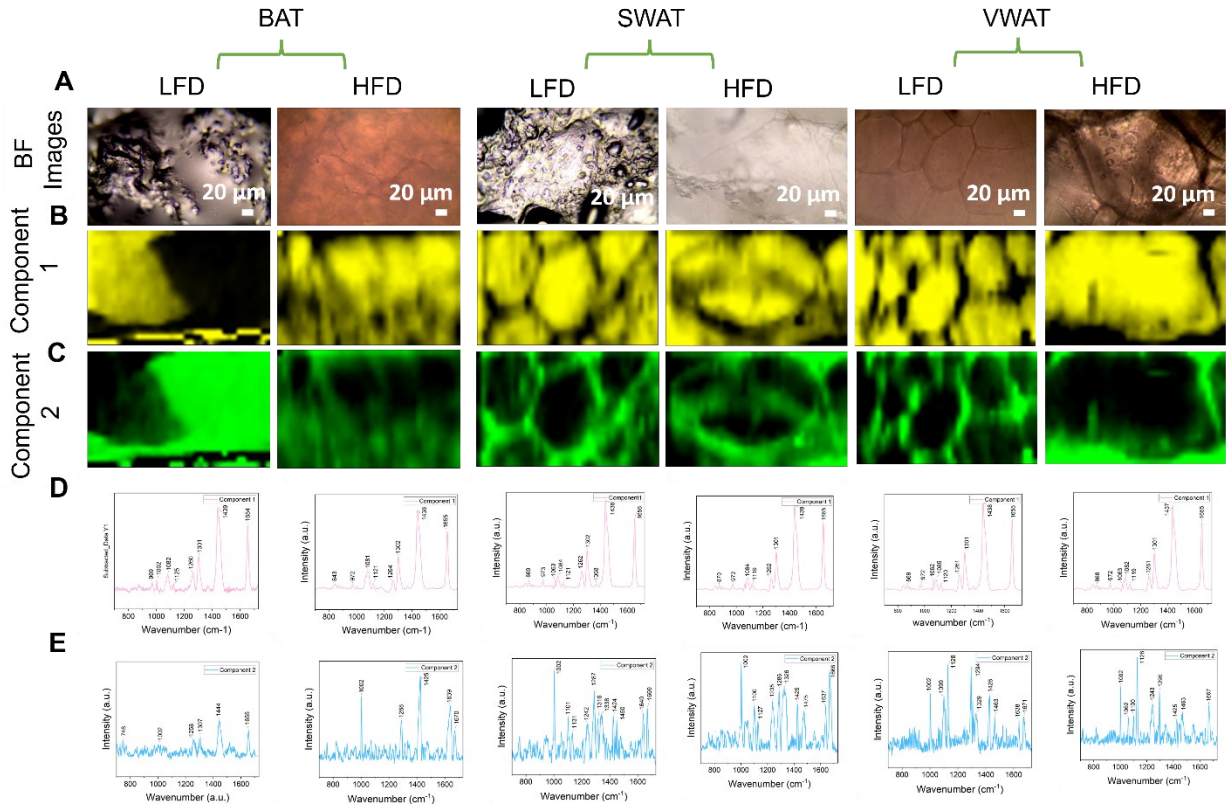

Figure 7. *Representative Raman mapping images analyzed by Empty Modelling showing lipid profile changes between LFD and HFD groups of fresh samples. (A) Bright-field images represent*

lipid structures in (A) BAT, SWAT, and VWAT. Generated Raman mapped images of LFD and HFD groups showing (B) component 1 and (C) component 2, which show chemical species within the adipocytes and at the cell membrane, respectively. Extracted Raman spectra from the corresponding images for each element (D) component 1 and (E) component 2. The Scalebar = 20 µm.

To perform targeted lipidomics analysis, we applied the Direct Classical Least Squares (DCLS) analysis to compare the profile of ω-3 and ω-6 fatty acids within the adipose tissues before and after HFD. This technique is appropriate when we have a reference spectrum for the component we are profiling. After entering the reference spectrum, the method finds the similarity between the reference spectrum and the Raman spectra collected from each part of the scanned image (at each pixel), followed by a generated image showing the match score for the molecule of interest. We built a library of Raman spectra comprising the most abundant ω-3 and ω-6 fatty acids (α-Linoleic acid, Docosahexaenoic acid, Docosapentaenoic acid, Eicosapentaenoic acid, Stearidonic acid, Arachidonic acid, Linoleic acid, Oleic acid, and Cholesterol, Cholesteryl palmitate, 1,2-Dipalmitoyl-sn-glycero-3-phosphate sodium salt, and Glyceryl tripalmitate) in the adipose tissues. **Figures S7A-S7C** to **Figure S10A-S10C** represent Raman mapping images of ω-3 fatty acids such as α-Linoleic acid (α-LA), Stearidonic acid (SDA), Eicosapentaenoic acid (EPA), Docosapentaenoic acid (DPA), and Docosahexaenoic acid (DHA) for BAT, SWAT, and VWAT tissues in LFD and HFD groups of both FFPE and fresh samples. In each generated mapping image, the brighter color corresponds to a higher level of fatty acids, and the darker color corresponds to a lower level of the same fatty acids. According to the Raman images, all the mentioned fatty acids were expressed mainly within the cytoplasm of the adipose tissues. We compared the score of fatty acids (representing the relative concentration of the fatty acids) for the LFD and HFD groups in BAT, SWAT, and VWAT tissues (**Figures 8A-8C**). The level of α-Linoleic Acid, Stearidonic Acid, Eicosapentaenoic Acid, Docosapentaenoic Acid, and Docosahexaenoic Acid were elevated in BAT tissues, while level of these fatty acids were reduced in SWAT and VWAT tissues of HFD group compared to LFD group (see the ratio in Table S4 of the *Supporting Information*).

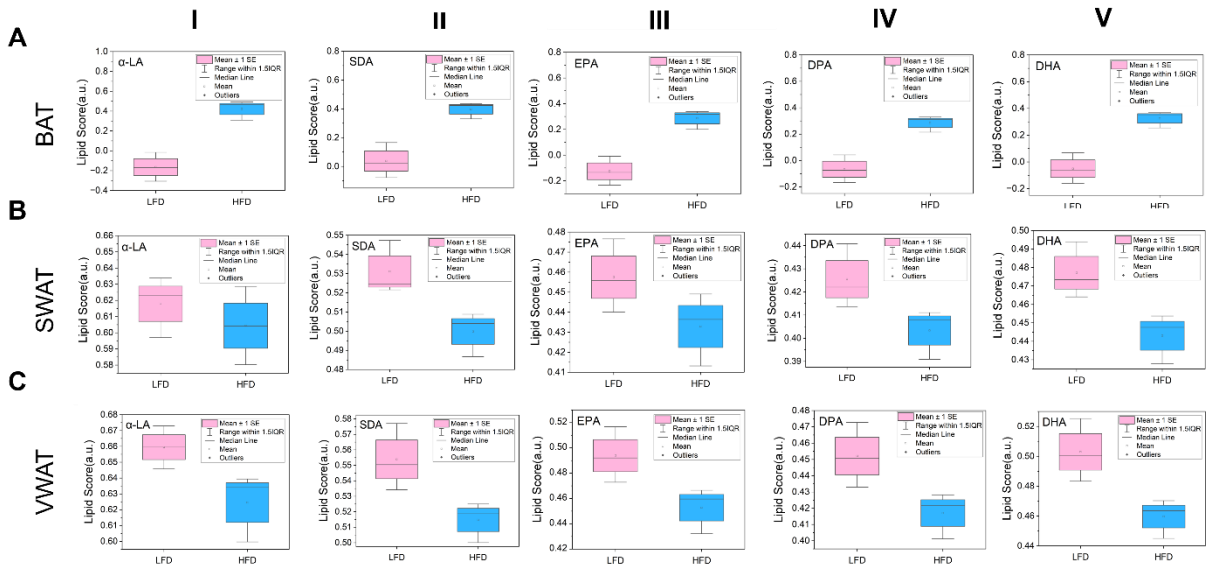

Figure 8. *The box plots, derived from images analyzed by the DCLS method, show the mean value corresponding to (I) α-Linoleic acid (α-LA), (II) Stearidonic acid (SDA), (III) Eicosapentaenoic acid (EPA), (IV) Docosapentaenoic acid (DPA), and (V) Docosahexaenoic acid (DHA) variation between LFD and HFD of (A) BAT, (B) SWAT, and (C) VWAT.*

Further, we performed DCLS analysis of ω-6 fatty acids such as Linoleic Acid (LA), Arachidonic Acid (AA), Phosphatic Acid (PA), and ω-9 fatty acid, Oleic Acid (OA) for both FFPE and fresh samples of BAT, SWAT, and VWAT tissues (**Figures S11A-S11C** to **Figures S14A-S14C**). According to the results, all the mentioned fatty acids were expressed mainly in the cytoplasm of the adipocytes. The comparison of the levels of PA between the LFD and HFD groups showed a higher level of this fatty acid in the HFD group for all tissue types, including BAT, SWAT, and VWAT tissues. While the levels of LA, AA, and OA increased in HFD compared to LFD for the BAT tissues, these fatty acids were found to be lower in HFD compared to LFD for SWAT and VWAT tissues (**Figures 9A-9C).** The mean value of these fatty acids can be seen in Table S4.

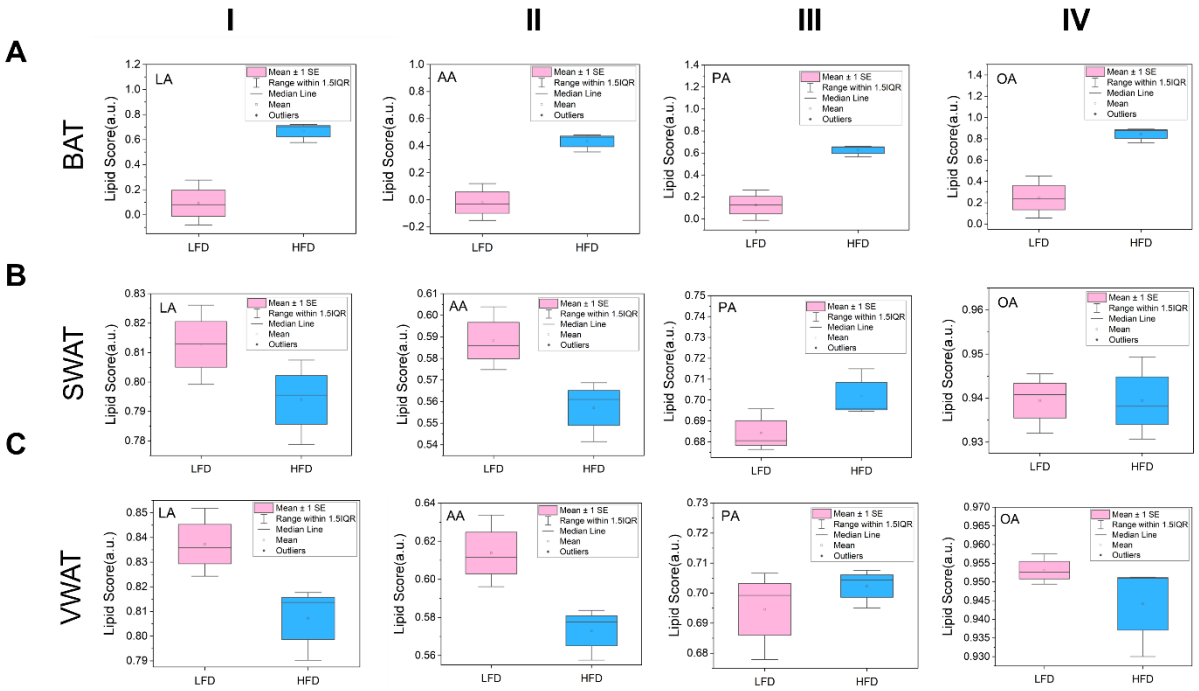

Figure 9. *The box plots, derived from images analyzed by the DCLS method, show the mean values corresponding to (I) Linoleic Acid (LA), (II) Arachidonic Acid (AA), (III) Phosphatic Acid (PA), and (IV) Oleic Acid (OA) variation between LFD and HFD of (A) BAT, (B) SWAT, and (C) VWAT tissues.*

Moreover, due to the importance of cholesterol (Chol) and triacylglycerols (TG) and the correlation between adipose tissue dysfunction and cholesterol imbalance, Raman images were analyzed using DCLS for these fatty acids. **Figures S15A-S15C** to **Figures S18A-S18C** Raman mapping images show the distribution of cholesterol, cholesterol-ester (Chol-E), and triacylglycerols in the adipocytes of BAT, SWAT, and VWAT for both FFPE and fresh samples. The HFD group showed larger lipid droplets containing Chol, Chol-E, and TG compared to the LFD groups. Chol, Chol-E, and TG levels were significantly elevated in the HFD group of VWAT, SWAT, and BAT tissues compared to LFD group (**Figure 10A-10C)**. Table S4 shows the mean value for these fatty acids.

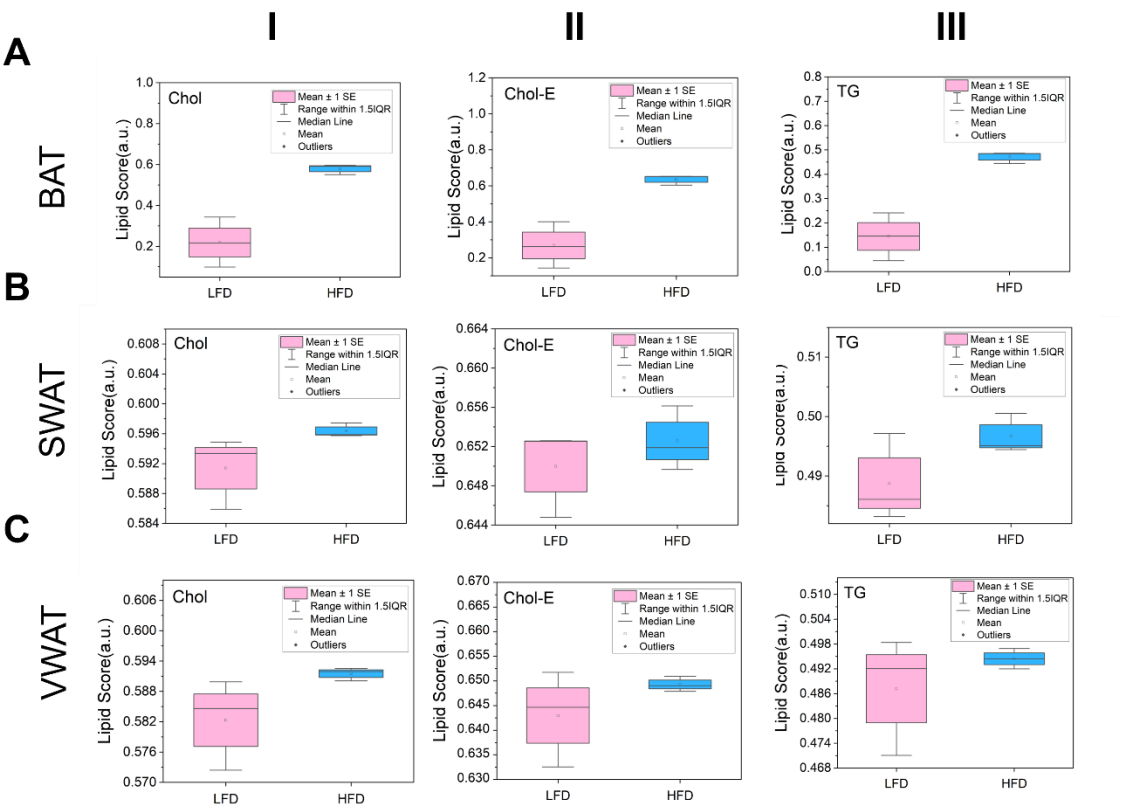

Figure 10. *The box plots, derived form images analyzed by the DCLS method, show the mean values corresponding to (I) Cholesterol (Chol), (II) Cholesterol Ester (Chol-E), and (III) triacylglycerol (TG) variation between LFD and HFD groups of (A) BAT, (B) SWAT, and (C) VWAT tissues.*

Figure 11A shows that in competition between α-LA and LA within HFD group, LA which is a metabolite of ω-6 fatty acids is higher than α-LA which is metabolite of ω-3 fatty acids. Higher content of LA led to higher content of AA which is associated to inflammatory status compared to DHA, **Figure 11B**. Furthermore, a comparison of ω-6/ω-3 fatty acid ratio provided by LC-MS method for all tissues, indicated a higher ratio for HFD tissues compared to LFD counterparts. Within the HFD group, BAT tissues showed a higher ratio in contrast to SWAT and VWAT tissues, **Figure 11C**.

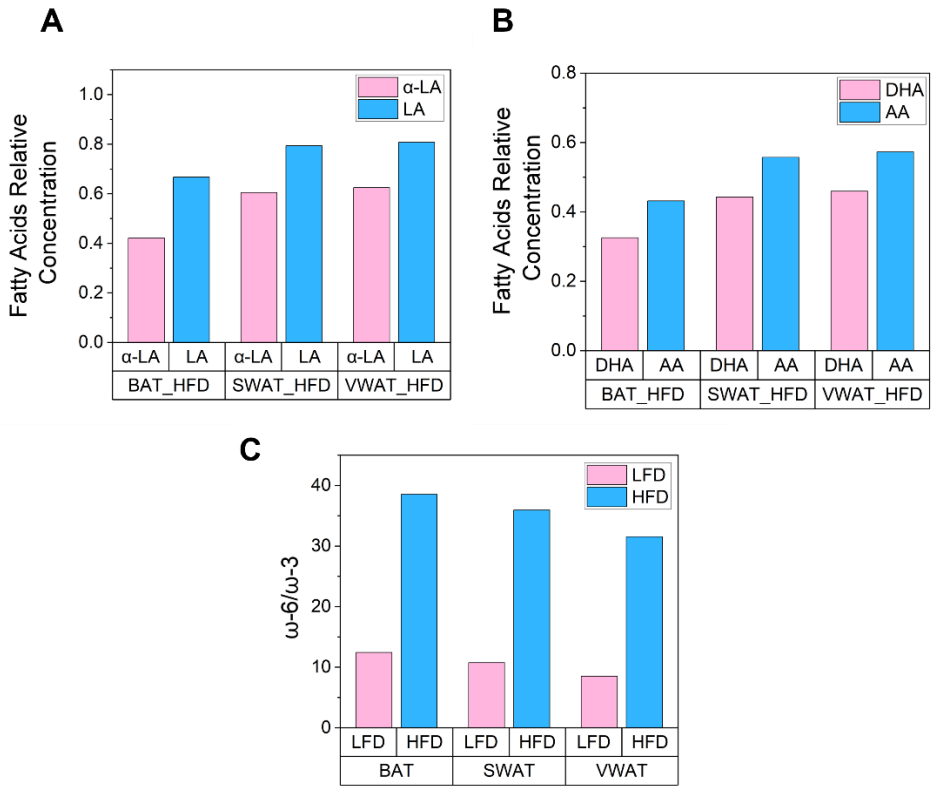

Figure 11. *Comparison of (A) Arachidonic Acid (AA) and Docosahexaenoic acid (DHA) (B) α-Linoleic acid and Linoleic acid (LA) (C) ω-6/ω-3 ratio for all tissues for BAT, SWAT, and VWAT tissues. Figure (A) and (B) were generated by the DCLS data of Raman mapping image and Figure (C) were generated by the LC-MS results.*

DISCUSSIONS AND CONCLUSIONS

In this research, we have demonstrated that immunohistochemistry results coupled with Raman spectroscopy and microscopy are efficient methods for identifying cellular alterations in the adipose tissues induced by a high-fat diet. The high-fat diet resulted in the hypertrophy of adipocytes in BAT, SWAT, and VWAT, as evidenced by the H&E image analysis. The hypertrophy of adipocytes is recognized as a critical phenomenon in the dysfunction of the adipose tissue, causing reduced oxygen levels and inflammation and ultimately giving rise to metabolic disorders [46]. Our results from picrosirius red (PSR)-stained imaging indicated that HFD increased collagen levels, leading to fibrosis and deposition of extracellular matrix (ECM) proteins in BAT, SWAT, and VWAT. Studies suggested that when the size of adipocytes in white

adipose tissue reaches a specific threshold, further additional enlargement of the adipocytes could impair their metabolism [40, 41]. Developing fibrosis within adipose tissue could be a defensive mechanism to restrict excessive enlargement beyond this critical point [41]. This, in turn, helps mitigate metabolic dysfunction in adipocytes [40]. Other studies indicate that in response to hypoxic conditions during fibrosis, the ECM expresses genes involved in its remodeling and, potentially contributing to the progression of the disease [47]. We visualize cellular dynamics in adipose tissue through a closer look at crown-like structures. Examining adipocyte size and crown-like structure (CLS) density through H&E and IHC staining revealed a compelling connection. Our images suggest a direct positive correlation, with larger adipocytes surrounded by a greater number of CLS. This finding aligns with previous research, hinting that macrophage infiltration is triggered by expanding adipocytes [48]. The presence of Iba1-positive crown-like structures in IHC images pointed towards a potential role of immune cells in adipocyte dynamics [38, 49]. Our results revealed a striking difference in crown-like structures (CLS) across adipose tissues. As visualized in the IHC images (e.g., **Figure 4A, 4D, 4F** showing CLS in HFD VWAT and LFD VWAT), HFD-fed animals exhibited significantly higher CLS density compared to their LFD counterparts, particularly within visceral white adipose tissue (VWAT). This suggests that a high-fat diet disproportionately impacts VWAT, promoting macrophage infiltration and potentially indicating localized inflammation (**Figure 4H**).

However, interestingly, BAT and SWAT tissues showed no significant difference in CLS density in the HFD groups. This implies that, in these specific depots of BAT and SWAT, HFD consumption might not directly accelerate adipocyte death or trigger the same inflammatory response observed in VWAT. During inflammation, locally secreted chemokines (e.g., CCL2 and CXCL12) act as sirens, attracting macrophages. These macrophages gather around struggling adipocytes, forming what we call crown-like structures. From within these structures, macrophages release inflammatory cytokines, potentially contributing to insulin resistance [50, 51]. To gain deeper insights into the impact of adipocyte hypertrophy on lipid composition and lipid metabolism, we employed Raman spectroscopy and microscopy to analyze fatty acid and lipid profiles in BAT, SWAT, and VWAT tissues [36]. We unveil the spatial distribution and composition of lipid

profiles with Raman imaging. While the overall Raman spectra of adipose tissues from both LFD and HFD groups appeared similar, a closer look at the molecular level revealed fascinating differences. Leveraging the power of Raman imaging, a non-invasive technique, we generated insightful qualitative and quantitative data on fatty acid and lipid profiles within these tissues. Using Empty modeling and direct classical least squares (DCLS) methods, we constructed Raman map images showcasing the spatial distribution of specific lipids. Each pixel of these Raman images reflects the relative abundance of different molecules (**Figures 8-10**). These detailed analyses revealed significant changes in visceral white adipose tissue (VWAT). The Raman maps and quantitative analysis specifically pointed to elevated levels of cholesterol ester, cholesterol, and triacylglycerols in HFD VWAT tissues compared to LFD. Raman imaging of adipose tissues indicated that a significant portion of the volume in HFD BAT, SWAT, and VWAT adipocytes is filled by large lipid droplets. These results are in agreement with the results of H&E images. According to the Raman images, all the mentioned fatty acids were expressed mainly within the cytoplasm of the adipose tissues. In addition, The quantitative analysis of the Raman maps pointed to elevated levels of ω-3, ω-6, ω-9, PA, Chol, Chol-E, and TG in HFD tissues compared to LFD. This rise in fatty acid levels may be attributed to the enlargement of the fat pads. Moreover, the statistical analysis of Raman spectra indicates that HFD feeding significantly increases lipid unsaturation within BAT, SWAT, and VWAT tissues. This increase in the level of unsaturated lipids and ω-6 fatty acids level in the HFD samples could be considered an indicator of inflammation, mainly connected to the synthesis pathway of eicosanoid and conversion of DGLA into AA [52]. In summary, a high-fat diet might disproportionately impact lipid metabolism and accumulation in VWAT compared to other fat depots, aligning with human data [53].

Acknowledgment

M.R.G. was supported by the National Science Foundation (NSF CAREER award number: 2045640). Research reported in this publication was supported by the National Institute of General Medical Sciences of the National Institutes of Health under award number R35GM150564. This project utilized the Cell Biology and Bioimaging Core that is supported in

part by COBRE (P20 GM135002 & P20 GM103528) and NORC (P30 DK072476) center grants from the National Institutes of Health. Confocal Raman spectroscopy and microscopy was performed at the Shared Instrumentation Facility (SIF) at Louisiana State University.

REFERENCES

1. Ouchi, N., et al., *Adipokines in inflammation and metabolic disease.* Nature reviews immunology, 2011. **11**(2): p. 85-97.
2. Chooi, Y.C., C. Ding, and F. Magkos, *The epidemiology of obesity.* Metabolism, 2019. **92**: p. 6-10.
3. Donjuán-Loredo, G., et al., *Raman spectroscopy for adipose tissue assessment in rat models of obesity and type 1 diabetes.* Applied Spectroscopy, 2021. **75**(9): p. 1189-1197.
4. Sun, K., et al., *Endotrophin triggers adipose tissue fibrosis and metabolic dysfunction.* Nature communications, 2014. **5**(1): p. 3485.
5. Czamara, K., et al., *Raman studies of the adipose tissue: Current state-of-art and future perspectives in diagnostics.* Progress in Lipid Research, 2022: p. 101183.
6. Simopoulos, A.P., *An increase in the omega-6/omega-3 fatty acid ratio increases the risk for obesity.* Nutrients, 2016. **8**(3): p. 128.
7. Tanaka, M., et al., *Molecular mechanism of obesity-induced 'metabolic'tissue remodeling.* Journal of Diabetes Investigation, 2018. **9**(2): p. 256-261.
8. Dugail, I., et al., *New insights into how adipocytes sense their triglyceride stores. Is cholesterol a signal?* Hormone and metabolic research, 2003. **35**(04): p. 204-210.
9. Frayn, K.N., P. Arner, and H. Yki-Järvinen, *Fatty acid metabolism in adipose tissue, muscle and liver in health and disease.* Essays in biochemistry, 2006. **42**: p. 89-103.
10. Simopoulos, A.P., *Evolutionary aspects of the dietary omega-6/omega-3 fatty acid ratio: medical implications.* Evolutionary Thinking in Medicine: From Research to Policy and Practice, 2016: p. 119-134.
11. Burdge, G.C. and P.C. Calder, *Introduction to fatty acids and lipids.* Intravenous Lipid Emulsions, 2015. **112**: p. 1-16.
12. Simopoulos, A.P., *Omega-3 fatty acids in health and disease and in growth and development.* The American journal of clinical nutrition, 1991. **54**(3): p. 438-463.
13. Nagy, K. and I.-D. Tiuca, *Importance of fatty acids in physiopathology of human body*, in *Fatty acids*. 2017, IntechOpen.
14. Raj, R.R., S. Lofquist, and M.-J. Lee, *Remodeling of adipose tissues by fatty acids: Mechanistic update on browning and thermogenesis by n-3 polyunsaturated fatty acids.* Pharmaceutical Research, 2023. **40**(2): p. 467-480.
15. Yu, B.L., S.P. Zhao, and J.R. Hu, *Cholesterol imbalance in adipocytes: a possible mechanism of adipocytes dysfunction in obesity.* Obesity Reviews, 2010. **11**(8): p. 560-567.
16. Krause, B.R. and A.D. Hartman, *Adipose tissue and cholesterol metabolism.* Journal of lipid research, 1984. **25**(2): p. 97-110.
17. Murphy, R.C., J. Fiedler, and J. Hevko, *Analysis of nonvolatile lipids by mass spectrometry.* Chemical reviews, 2001. **101**(2): p. 479-526.
18. Cajka, T. and O. Fiehn, *Comprehensive analysis of lipids in biological systems by liquid chromatography-mass spectrometry.* TrAC Trends in Analytical Chemistry, 2014. **61**: p. 192-206.
19. Tian Jr, H., et al., *Fluorescent probes for the imaging of lipid droplets in live cells.* Coordination Chemistry Reviews, 2021. **427**: p. 213577.
20. Sezgin, E. and P. Schwille, *Fluorescence techniques to study lipid dynamics.* Cold Spring Harbor perspectives in biology, 2011. **3**(11): p. a009803.
21. Li, M., et al., *Alkyne-and nitrile-anchored gold nanoparticles for multiplex SERS imaging of biomarkers in cancer cells and tissues.* Nanotheranostics, 2019. **3**(1): p. 113.
22. Bishop, D.P., et al., *A guide to integrating immunohistochemistry and chemical imaging.* Chemical Society Reviews, 2018. **47**(11): p. 3770-3787.
23. Angelo, M., et al., *Multiplexed ion beam imaging of human breast tumors.* Nature medicine, 2014. **20**(4): p. 436-442.
24. Chaichi, A., et al., *Label-free lipidome study of paraventricular thalamic nucleus (PVT) of rat brain with post-traumatic stress injury by Raman imaging.* Analyst, 2021. **146**(1): p. 170-183.

25. Kelley, D.P., et al., *Labelfree mapping and profiling of altered lipid homeostasis in the rat hippocampus after traumatic stress: Role of oxidative homeostasis.* Neurobiology of stress, 2022. **20**: p. 100476.
26. Ohira, S., et al., *Label-free detection of myocardial ischaemia in the perfused rat heart by spontaneous Raman spectroscopy.* Scientific reports, 2017. **7**(1): p. 42401.
27. Haifler, M., et al., *Discrimination of malignant and normal kidney tissue with short wave infrared dispersive Raman spectroscopy.* Journal of biophotonics, 2018. **11**(6): p. e201700188.
28. Mehta, N., et al., *Multimodal Label-Free Monitoring of Adipogenic Stem Cell Differentiation Using Endogenous Optical Biomarkers.* Advanced functional materials, 2021. **31**(43): p. 2103955.
29. Rygula, A., et al., *Raman spectroscopy of proteins: a review.* Journal of Raman Spectroscopy, 2013. **44**(8): p. 1061-1076.
30. Czamara, K., et al., *Raman spectroscopy of lipids: a review.* Journal of Raman spectroscopy, 2015. **46**(1): p. 4-20.
31. Kochan, K., et al., *Pathological changes in the biochemical profile of the liver in atherosclerosis and diabetes assessed by Raman spectroscopy.* Analyst, 2013. **138**(14): p. 3885-3890.
32. Sheikh, E., et al., *Multimodal Imaging of Pancreatic Cancer Microenvironment in Response to an Antiglycolytic Drug.* Advanced Healthcare Materials, 2023: p. 2301815.
33. Abramczyk, H., et al., *The role of lipid droplets and adipocytes in cancer. Raman imaging of cell cultures: MCF10A, MCF7, and MDA-MB-231 compared to adipocytes in cancerous human breast tissue.* Analyst, 2015. **140**(7): p. 2224-2235.
34. Kochan, K., et al., *Raman spectroscopy analysis of lipid droplets content, distribution and saturation level in Non-Alcoholic Fatty Liver Disease in mice.* Journal of biophotonics, 2015. **8**(7): p. 597-609.
35. Majka, Z., et al., *Prominent hypertrophy of perivascular adipocytes due to short-term high fat diet.* Biochimica et Biophysica Acta (BBA)-Molecular Basis of Disease, 2022. **1868**(2): p. 166315.
36. Czamara, K., et al., *Raman spectroscopy as a novel tool for fast characterization of the chemical composition of perivascular adipose tissue.* Analyst, 2018. **143**(24): p. 5999-6005.
37. Ruiz-Ojeda, F.J., et al., *Extracellular matrix remodeling of adipose tissue in obesity and metabolic diseases.* International journal of molecular sciences, 2019. **20**(19): p. 4888.
38. Murano, I., et al., *Dead adipocytes, detected as crown-like structures, are prevalent in visceral fat depots of genetically obese mice.* Journal of lipid research, 2008. **49**(7): p. 1562-1568.
39. Jones, J.E., et al., *The adipocyte acquires a fibroblast-like transcriptional signature in response to a high fat diet.* Scientific Reports, 2020. **10**(1): p. 2380.
40. Muir, L.A., et al., *Adipose tissue fibrosis, hypertrophy, and hyperplasia: Correlations with diabetes in human obesity.* Obesity, 2016. **24**(3): p. 597-605.
41. Divoux, A., et al., *Fibrosis in human adipose tissue: composition, distribution, and link with lipid metabolism and fat mass loss.* Diabetes, 2010. **59**(11): p. 2817-2825.
42. Rittié, L., *Method for picrosirius red-polarization detection of collagen fibers in tissue sections.* Fibrosis: methods and protocols, 2017: p. 395-407.
43. Boi, S.K., et al., *Obesity alters immune and metabolic profiles: New insight from obese-resistant mice on high-fat diet.* Obesity, 2016. **24**(10): p. 2140-2149.
44. Bruun, J.M., et al., *Monocyte chemoattractant protein-1 release is higher in visceral than subcutaneous human adipose tissue (AT): implication of macrophages resident in the AT.* The Journal of clinical endocrinology & metabolism, 2005. **90**(4): p. 2282-2289.
45. Majzner, K., et al., *Raman imaging providing insights into chemical composition of lipid droplets of different size and origin: in hepatocytes and endothelium.* Analytical chemistry, 2014. **86**(13): p. 6666-6674.
46. Liu, F., et al., *Adipose morphology: a critical factor in regulation of human metabolic diseases and adipose tissue dysfunction.* Obesity surgery, 2020. **30**: p. 5086-5100.
47. Halberg, N., et al., *Hypoxia-inducible factor 1α induces fibrosis and insulin resistance in white adipose tissue.* Molecular and cellular biology, 2009.
48. Weisberg, S.P., et al., *Obesity is associated with macrophage accumulation in adipose tissue.* The Journal of clinical investigation, 2003. **112**(12): p. 1796-1808.
49. Poret, J.M., et al., *High fat diet consumption differentially affects adipose tissue inflammation and adipocyte size in obesity-prone and obesity-resistant rats.* International journal of obesity, 2018. **42**(3): p. 535-541.
50. Wu, D., et al., *Eosinophils sustain adipose alternatively activated macrophages associated with glucose homeostasis.* Science, 2011. **332**(6026): p. 243-247.
51. Shoelson, S.E., J. Lee, and A.B. Goldfine, *Inflammation and insulin resistance.* The Journal of clinical investigation, 2006. **116**(7): p. 1793-1801.
52. Czamara, K., et al., *Lipid droplets formation represents an integral component of endothelial inflammation induced by LPS.* Cells, 2021. **10**(6): p. 1403.

53. Wrzosek, M., et al., *Impact of fatty acids on obesity-associated diseases and radical weight reduction.* Obesity surgery, 2022: p. 1-13.